

# Surface-wave interferometry on single subwavelength slit-groove structures fabricated on gold films

F. Kalkum\* and G. Gay, O. Alloschery, J. Weiner  
*IRSAMC/LCAR*  
*Université Paul Sabatier, 118 route de Narbonne,*  
*31062 Toulouse, France*

H. J. Lezec  
*Centre National de la Recherche Scientifique, 3, rue Michel-Ange, 75794 Paris cedex 16, France and*  
*Thomas J. Watson Laboratories of Applied Physics,*  
*California Institute of Technology, Pasadena, California 91125 USA*

Y. Xie, M. Mansuripur  
*College of Optical Sciences, University of Arizona, Tucson, Arizona 85721 USA*  
 (Dated: October 10, 2018)

We apply the technique of far-field interferometry to measure the properties of surface waves generated by two-dimensional (2D) single subwavelength slit-groove structures on gold films. The effective surface index of refraction  $n_{\text{surf}}$  measured for the surface wave propagating over a distance of more than  $12 \mu\text{m}$  is determined to be  $n_{\text{surf}} = 1.016 \pm 0.004$ , to within experimental uncertainty close to the expected bound surface plasmon-polariton (SPP) value for a Au/Air interface of  $n_{\text{spp}} = 1.018$ . We compare these measurements to finite-difference-time-domain (FDTD) numerical simulations of the optical field transmission through these devices. We find excellent agreement between the measurements and the simulations for  $n_{\text{surf}}$ . The measurements also show that the surface wave propagation parameter  $k_{\text{surf}}$  exhibits transient behavior close to the slit, evolving smoothly from greater values asymptotically toward  $k_{\text{spp}}$  over the first 2-3  $\mu\text{m}$  of slit-groove distance  $x_{\text{sg}}$ . This behavior is confirmed by the FDTD simulations.

PACS numbers: 42.25.Fx. 73.20.Mf. 78.67.-n  
 Keywords: plasmon; surface wave; nanostructure

## I. INTRODUCTION

Recent measurements [1, 2] have characterized surface waves arising from optical excitation of a series of subwavelength slit-groove structures fabricated on silver films. The amplitude, wavelength and phase of these surface waves have been measured over a slit-groove distance of a few microns. After an initial rapid amplitude decrease extending to  $\sim 3 \mu\text{m}$  from the slit edge, the interference fringe persists over several microns with a near-constant amplitude and a contrast  $\simeq 0.3$ . The “near-zone” of rapidly changing surface wave character indicates initial transient phenomena, while the longer-range “far-zone” settling to constant amplitude and contrast is the signature of a guided mode surface plasmon polariton (SPP). The measured interference fringe wavelength  $\lambda_{\text{surf}} = 814 \pm 8 \text{ nm}$  resulted in the determination of an effective index of refraction  $n_{\text{surf}} = 1.047$ , significantly higher than expected from conventional theory [3],  $n_{\text{spp}} = 1.015$ . The question naturally arose as to whether this result is simply a consequence of interference fringe sampling over an interval predominantly in a transient near-zone peculiar to silver films, or was related to the specific surface properties of the silver films deposited on fused silica [4], or may indicate a more *generic* phenomenon related to the transient properties of surface waves, generated by subwavelength slits, within 2-3 wavelengths of the edge of origin. Subsequent investigation of the physical-chemical properties of the silver films confirmed that they were free of surface contaminants, and FDTD simulations showed excellent agreement with the experimental results in silver films [5, 6].

In order to explore these surface waves further we have carried out a series of experiments similar to those already reported but using evaporated gold films instead of silver. We performed only “output-side” experiments [1] because they yield a phase modulated interference fringe less susceptible to noise than the amplitude modulation signal of the “input-side” experiments [2]. In addition we have compared the measurements to detailed field amplitude and

---

\*Permanent address: Physikalisches Institut, Universität Bonn, Wegelerstrasse 8, 53115 Bonn, Germany

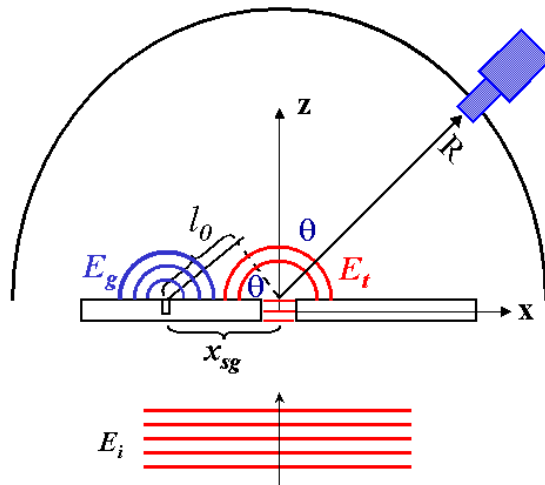


FIG. 1: Diagram showing interfering wavefronts, optical path difference between  $E_t$  and  $E_g$ , and far-field detection. Slit dimensions are 100 nm width, 20  $\mu\text{m}$  length. Groove dimensions are 100 nm width, 100 nm nominal depth, 20  $\mu\text{m}$  length. The evaporated gold layer deposited on a 1 mm fused silica substrate has a 400 nm nominal thickness.

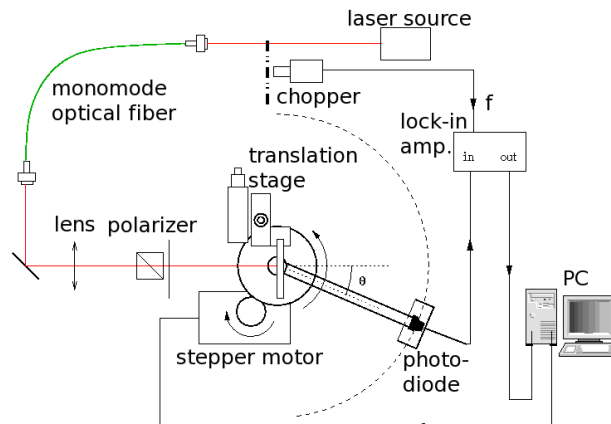


FIG. 2: Goniometer setup for measuring far-field light intensity and angular distributions. See text for description.

phase maps generated by FDTD numerical solutions [7, 8] to the Maxwell equations in the vicinity of the slit-groove structure. Both experiments and FDTD simulation show that the surface wave exhibits transient properties in wavelength and amplitude in the near-zone. This transient behavior can be interpreted in terms of surface modes all of which dissipate beyond the near-zone except for  $k_{\text{spp}}$ , the bound surface mode.

## II. EXPERIMENTAL SETUP

The structures were fabricated with a focused ion beam (FIB) station as described previously in [2]. The experiments were performed on the same home-built goniometer setup used in the silver studies. For convenience, Figs. 1,2 of [1] are reproduced here to show the principle of the measurement and the schematic arrangement of the apparatus. Output from a temperature stabilized diode laser source, is modulated at 850 Hz by a mechanical chopper, injected into a monomode optical fibre, focused and linearly polarized (TM polarization, H-field parallel to the slit long axis) before impinging perpendicularly on the matrix of structures mounted in a sample holder. The beam waist diameter and confocal parameter of the illuminating source are 300  $\mu\text{m}$  and 33 cm, respectively. The sample holder itself is fixed to a precision x-y translator, and individual slit-groove structures of the 2-D matrix are successively positioned at the laser beam waist. A photodiode detector is mounted at the end of a 200 mm rigid arm that rotates about

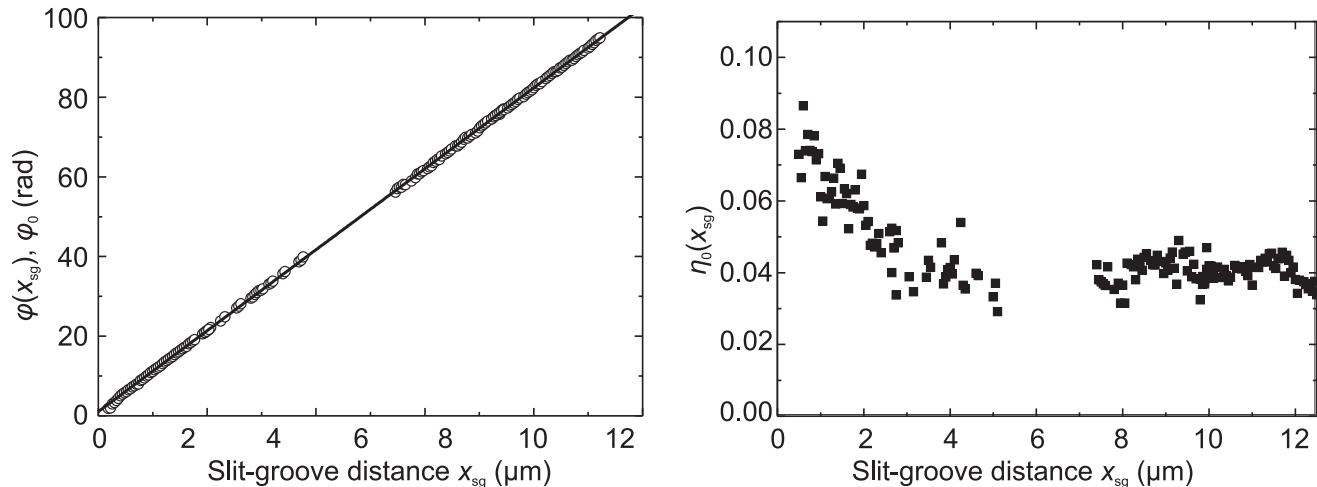


FIG. 3: Left panel: Points are the measured fringe phase  $\varphi(x_{\text{sg}})$  as a function of slit-groove distance  $x_{\text{sg}}$ . The straight-line fit is  $\varphi_0 = k_{\text{surf}}x_{\text{sg}} + \varphi_{\text{int}}$  with constant slope  $k_{\text{surf}}$  and intercept  $\varphi_{\text{int}}$ . Gap in the data in left and right panels of this figure and in the left and right panels of Fig. 4 is due to defective structures in this interval. Right panel: Fringe amplitude  $\eta_0 \simeq 1/2C$  as a function of  $x_{\text{sg}}$  where  $C$  is the interference fringe contrast.

the center of the sample holder. A stepper motor drives the arm at calibrated angular increments of 1.95 mrad per step, and the overall angular resolution of the goniometer is  $\simeq 4$  mrad. The photodetector output current passes to a lock-in amplifier referenced to the optical chopper wheel. Data are collected on a personal computer that also controls the goniometer drive.

### III. RESULTS AND ANALYSIS

#### A. Measurements

With the detector rotated perpendicular to the structure plane ( $\theta = 0$  in Figs. 1, 2) the expression for the normalized detected intensity  $I/I_0$  as a function of slit-groove distance  $x_{\text{sg}}$  is given by

$$\frac{I}{I_0} \propto 1 + \eta_o^2 + 2\eta_o \cos(k_x x_{\text{sg}} + \varphi_{\text{int}}) \quad (1)$$

where  $\eta_o$  is related to the fringe contrast  $C$  through

$$C = \frac{2\eta_o}{1 + \eta_o^2} \quad (2)$$

In the argument of the cosine term  $k_x = 2\pi/\lambda_{\text{eff}}$  relates the propagation parameter of the surface wave to the effective surface wavelength, and the “intrinsic phase”  $\varphi_{\text{int}}$  is any phase contribution not directly due to the propagation path length  $x_{\text{sg}}$ . It may be associated with phase shifts at the slit or groove structures. The interferometry measurements were carried out on 4 separate substrates, each substrate containing about 50 structures in which the the slit-groove separation was systematically varied from 50 nm to more than 12  $\mu\text{m}$  in increments of 50 nm. The left panel of Fig. 3 plots the measured interference fringe phase against the slit-groove distance  $x_{\text{sg}}$ . The fitted value for  $k_{\text{surf}} = 2\pi/\lambda_{\text{surf}}$  determines the effective surface index of refraction  $n_{\text{surf}}$ , and extrapolation to zero slit-groove distance  $x_{\text{sg}}$  determines the intrinsic phase  $\varphi_{\text{int}}$ . The fit from the left panel of Fig. 3 yields

$$n_{\text{surf}} = \frac{\lambda_0}{\lambda_{\text{surf}}} = 1.016 \pm 0.004 \quad \text{and} \quad \varphi_{\text{int}} = 0.35\pi \pm 0.01\pi \quad (3)$$

The right panel of Fig. 3 plots  $\eta_0$ , the amplitude factor of the interference term in Eq. 1, as a function of slit-groove distance. From Eq. 2 this amplitude factor can be expressed in terms of the fringe visibility or contrast  $C$  as

$$\eta_0 = \frac{1 - \sqrt{1 - C^2}}{C} \simeq \frac{1}{2}C, \quad C \ll 1 \quad (4)$$

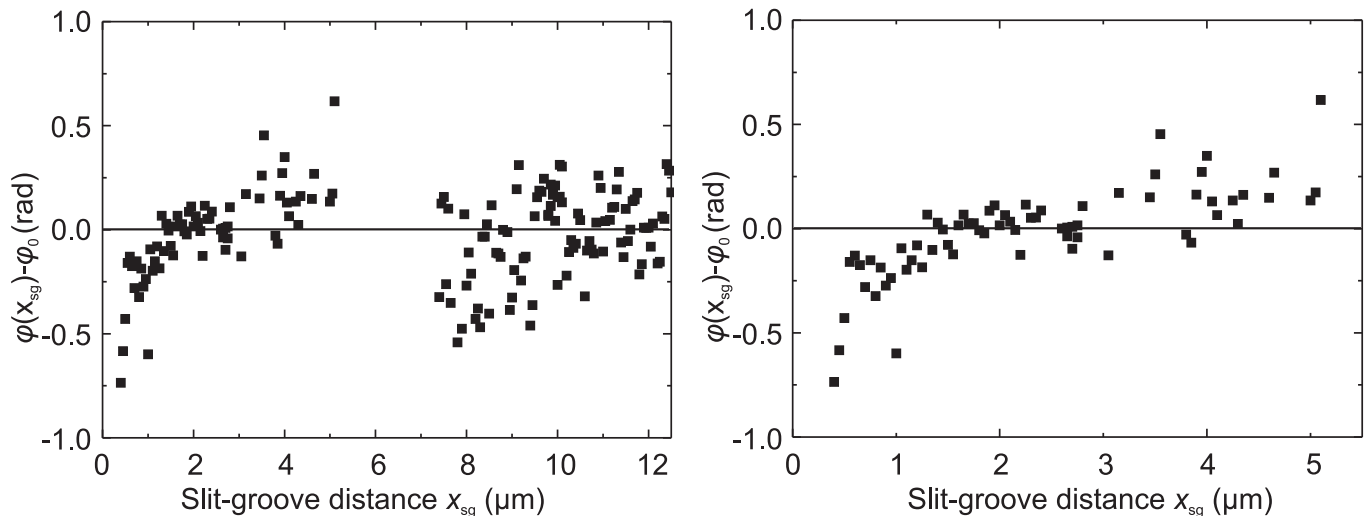


FIG. 4: Left panel: Fringe phase difference  $\varphi(x_{\text{sg}}) - \varphi_0$  as a function of slit groove distance  $x_{\text{sg}}$ . Deviation in the near-zone from  $\varphi_0$  indicates that early, transient fringe oscillation is slightly greater and approaches  $\varphi_0$  asymptotically in the far-zone beyond  $\sim 2 \mu\text{m}$  slit-groove distance. Right panel: Same data as shown in left panel but on an expanded scale of slit-groove distances to emphasize the curvature in  $\varphi(x_{\text{sg}}) - \varphi_0$  in the near-zone.

Although the fringe contrast shown in the right panel of Fig. 3 is about a factor of 5 below that measured for silver structures [1], the same rapid fall-off in the near-zone,  $x_{\text{sg}} \simeq 0 - 3 \mu\text{m}$ , followed by a near-constant contrast beyond is observed. This contrast behavior is evidence of surface-wave transient phenomena in the near-zone. More evidence of this transient behavior is shown in left and right panels of Fig. 4 that plot  $\varphi(x) - \varphi_0$  vs.  $x_{\text{sg}}$ , where  $\varphi_0 = k_{\text{surf}}x_{\text{sg}} + \varphi_{\text{int}}$  is the best-fit linear trace in the left panel of Fig. 3 over the range of slit-groove distances out to  $12 \mu\text{m}$ . A pronounced departure from the asymptotic value of  $\varphi_0$  is evident in the near-zone of slit groove distances, indicating that the fringe oscillation frequency is initially somewhat greater than the SPP value and smoothly decreases to it beyond the near-zone.

## B. Numerical simulations

The time-dependent Maxwell equations are solved numerically using an FDTD non-conformal grid refinement method in Cartesian space coordinates. The methodology is described in greater detail in Refs [7–9].

Figure 5 shows a field map of the  $z$ -component of the electric field amplitude, and Fig. 6 shows a field map of the  $y$ -component of the magnetic field amplitude. The  $|\mathbf{E}_z|$  map clearly shows the dipolar charge distribution concentrated at the corners of the slit on the input and output planes of the structure. These corner charge concentrations result from currents induced on the input side of the gold film by the magnetic field components  $|\mathbf{H}_y|$  shown in Fig. 6. The incident light propagates from below through the fused silica substrate onto the gold film and through the  $100 \text{ nm}$  wide,  $400 \text{ nm}$  thick slit. The incident light is TM polarized and the guided mode propagating along the  $\pm z$  direction within the slit sets up a standing wave resulting in a high  $|\mathbf{E}_z|$ ,  $|\mathbf{H}_y|$  amplitudes at the output plane. The groove is at the output side of the gold film; and, in the simulations depicted, the distance between the center of the slit and the center of the groove is  $3.18 \mu\text{m}$ . The absolute value of the  $z$ -component of the electric field amplitude  $|\mathbf{E}_z|$  just above (or just below) the gold film is proportional to the surface charge density at the film surface. Note that on the output side surface, in the region between the groove and the slit, the surface wave excited at the left edge of the slit travels to the groove, is reflected from the groove's right edge, then interferes with itself. The standing wave is clearly visible on and near the output side surface. Within the slit, on the vertical walls,  $\mathbf{E}_z$  is fairly strong as well. Here, however,  $\mathbf{E}_z$  is parallel to the metallic surface, and its presence within the skin depth of the slit walls does not signify the existence of surface charges; instead, the  $\mathbf{E}_z$ -field in this region is responsible for the surface currents that carry the charges back and forth between the entrance and exit facets of the slit. Figure 6 shows the magnitude of the magnetic field  $|\mathbf{H}_y|$  over the same region as Fig. 5. Interference fringes between the incident and reflected beams on fused silica substrate are clearly visible. Note also the interference fringes between the excited evanescent waves (mainly SPP) and the incident beam on the entrance facet of the gold film adjacent the substrate. Inside the slit,  $|\mathbf{H}_y|$  shows a dark band; this is caused by interference between the upward-moving guided mode within the slit and the reflected, downward-travelling mode.

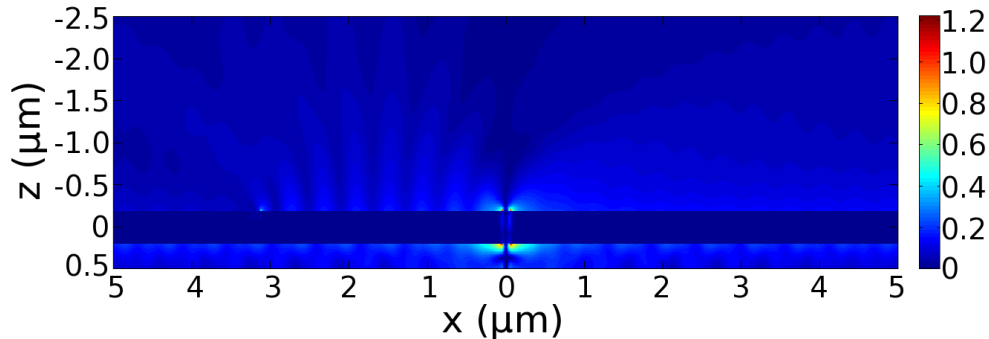


FIG. 5: FDTD simulations for slit-groove center-to-center distance of  $3.18 \mu\text{m}$ , slit and groove widths  $100 \text{ nm}$ , groove depth  $100 \text{ nm}$  and gold film thickness  $400 \text{ nm}$ . Map shows  $|E_z|$ ,  $z$ -components (perpendicular to input and output facets) of the electric field amplitude in the vicinity of the input and output surfaces.

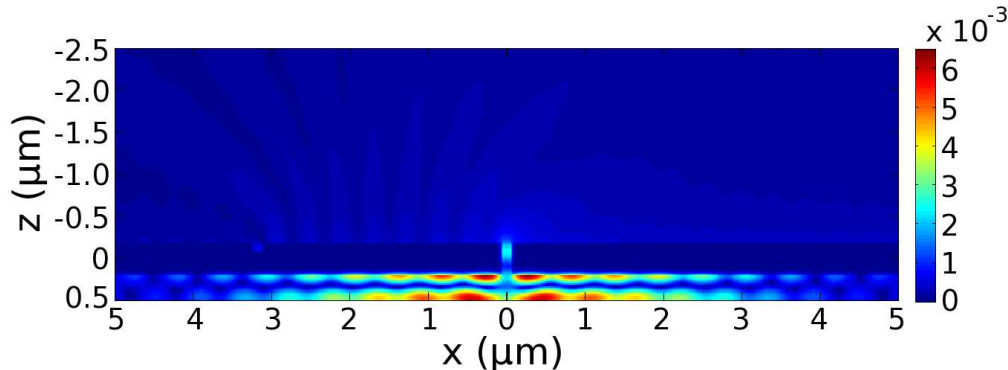


FIG. 6: FDTD simulations for slit-groove center-to-center distance of  $3.18 \mu\text{m}$ , slit and groove widths  $100 \text{ nm}$ , groove depth  $100 \text{ nm}$  and gold film thickness  $400 \text{ nm}$ . Map shows  $|H_y|$ ,  $y$ -components (parallel to the slit and groove long axis) of the magnetic field amplitude in the vicinity of the input and output surfaces.

In addition to the electric and magnetic field components  $E_z, H_y$  at the surface, the light transmission efficiency in the  $z$  direction through the slit as a function of slit-groove distance  $x_{\text{sg}}$  was calculated and is shown in Fig. 7. The transmission efficiency  $T$  is defined as the ratio of the  $z$ -component of the Poynting vector  $S_z^{\text{out}}$  on the output side, integrated over  $x$ , to the total energy flux incident on the slit  $S_z^{\text{in}}$ . The red trace plots the transmission efficiency  $T = S_z^{\text{out}}/S_z^{\text{in}}$  as a function of  $x_{\text{sg}}$  at the output plane. As expected the transmission efficiency exhibits pronounced oscillations with a rapid decrease in amplitude in the near-zone followed by a constant amplitude oscillation out to  $6 \mu\text{m}$ , the calculation limit. In the far-zone the blue trace fits the oscillations to a single cosine function,  $\cos[2(k_{\text{surf}}^{\text{fddd}} \cdot x_{\text{sg}} + \varphi_{\text{int}}^{\text{fddd}})]$ . These oscillations, as can be seen in Figs. 5 and 6, arise from the superposition of waves launched from the slit and back reflected at the groove. Because these waves are counterpropagating along  $x$ , rather than copropagating along  $z$ , the intensity fringe frequency is twice the fringe frequency of the far-field interferometry results expressed by Eq. 1. This standing wave at the output plane results in

$$T = S_z^{\text{out}}/S_z^{\text{in}} \propto 2 [1 + \cos 2(k_{\text{surf}}^{\text{fddd}} \cdot x_{\text{sg}} + \varphi_{\text{int}}^{\text{fddd}})] = 2 \{1 + \cos 2[\varphi(x_{\text{sg}})]\} \quad (5)$$

Taking into account this factor of two in the argument of the cos term, the fringe oscillation in the asymptotic far-zone is in good agreement with measurement and the expected SPP. In the near-zone the oscillation  $\varphi(x_{\text{sg}})$  exhibits a definite “chirp,” and Fig. 8 plots the deviation from the asymptotic value  $\varphi_0$  as function of  $x_{\text{sg}}$ . Comparing Fig. 8 to Fig. 4 we see that the FDTD results accord well with deviations in the interferometric fringes measured in the far-field.

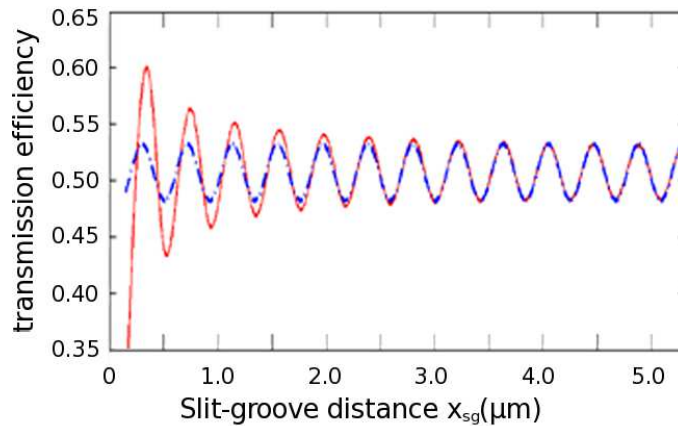


FIG. 7: FDTD calculations of the transmission efficiency  $T = S_z^{out}/S_z^{in}$  as a function of  $x_{sg}$ . Red curve traces  $T$ , and the blue curve traces a  $\cos(2k_{\text{surf}}^{\text{fdd}} \cdot x_{sg} + \varphi_{\text{int}}^{\text{fdd}})$  fit to the oscillation in the asymptotic region. Note the decreasing transmission amplitude in the near-zone close to the slit edge and the higher oscillation frequency compared to the asymptotic harmonic wave. Best-fit values for  $\lambda_{\text{surf}}^{\text{fdd}} = 2\pi/k_{\text{surf}}^{\text{fdd}} = 839$  nm and intrinsic phase  $\varphi_{\text{int}}^{\text{fdd}} = 0.55\pi$  rad.

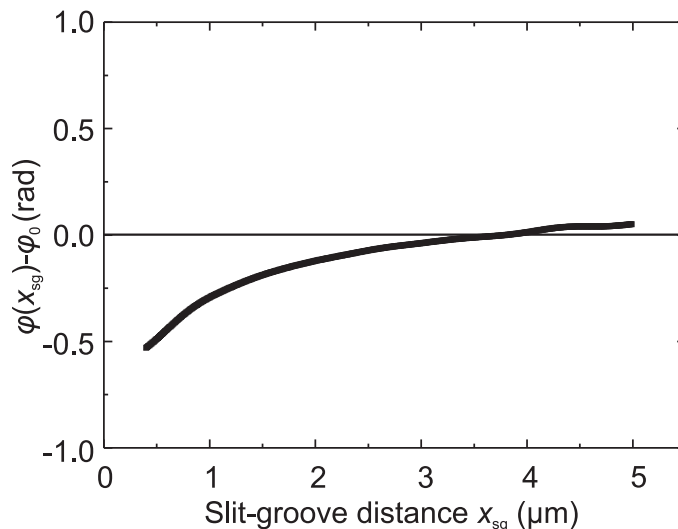


FIG. 8: Phase difference  $\varphi(x_{sg}) - \varphi_0$  as a function of  $x_{sg}$ , analogous to the right panel of Fig. 4 but derived from the FDTD simulation data. Residual “high frequency” oscillations in the phase difference, believed to be due to numeric artifacts in the FDTD results, have been smoothed.

## IV. DISCUSSION

### A. Surface wave in the far-zone

The index of refraction for the bound surface-plasmon-polariton  $n_{\text{spp}}$  is given by the Raether formula [3]

$$n_{\text{spp}} = \sqrt{\frac{\epsilon_m \epsilon_d}{\epsilon_m + \epsilon_d}} \quad (6)$$

where  $\epsilon_m$  and  $\epsilon_d$  are the real parts of the dielectric constants of metal and dielectric at the interface on which the surface wave propagates. Interpolation of reflectivity data for gold [10] at 852 nm yields  $\epsilon_{\text{Au}} = -28.82$  and from Eq. 6 the surface index of refraction for the surface plasmon polariton at the gold-air interface is  $\epsilon_{\text{spp}} = 1.018$ . The measured surface index of refraction reported here, to within experimental uncertainty and in the far-zone, is in accord with the SPP prediction. The results from the FDTD calculations are also in agreement with the experimental results and the SPP predictions. It appears therefore that in the far-zone, for both silver/air and gold/air surfaces, far-field interferometry and FDTD calculations show that the surviving long-range surface wave is indeed the expected bound

surface plasmon polariton. Table I summarizes the relevant parameters, far-field interferometric measurements, and finite-difference-time-dependent (FDTD) numerical simulations for gold and silver.

TABLE I: Summary of  $\lambda_{\text{surf}}$ ,  $n_{\text{surf}}$  and  $n_{\text{spp}}$  determined from far-field interferometric studies and FDTD simulations in gold and silver

	$\epsilon_m$	$\lambda_{\text{surf}}$	$n_{\text{surf}}$	$n_{\text{spp}}$
Au, Ref. [11]	-28.32	$839 \pm 6$ nm	$1.016 \pm 0.004$	1.018
Au, Ref. [12]	-31.62	839 nm	1.016	1.016
Ag, Ref. [13]	-33.27	$819 \pm 8$ nm	$1.04 \pm 0.01$	1.015
Ag, Ref. [14]	-33.27	$814 \pm 8$ nm	$1.05 \pm 0.01$	1.015
Ag, Ref. [15]	-33.98	837 nm	1.017	1.015

## B. Surface wave in the near-zone

In the near-zone both experiment and numerical simulation show that the surface wave deviates from pure SPP behavior. The effective propagation parameter  $k_x$ , originating near the slit edge, appears greater than  $k_{\text{spp}}$  and evolves smoothly to the bound mode over the near-zone interval of a few microns. This behavior may be interpreted either in terms of initial excitation of a composite evanescent surface “wave packet” in  $k$ -space at the slit edge [16], followed by subsequent decay of all surface modes except the bound  $k_{\text{spp}}$  mode or in terms of detailed field matching at the boundaries within the slit and near the slit edges [17]. These two points of view both invoke evanescent modes  $k_x \geq k_{\text{spp}}$  in order to satisfy boundary conditions in the vicinity of the slit edge, but standard wave-guide theory dictates that only the SPP mode is stable against phonon coupling to the bulk metal or to radiative decay. We can estimate the surface distance over which the dissipation occurs by appealing to the standard Drude model of a metal that expresses the frequency dependence of the dielectric constant  $\epsilon(\omega)$  in terms of the bulk plasmon resonance  $\omega_p$  and a damping constant  $\Gamma$ .

$$\epsilon(\omega) = \epsilon_0 \left( \epsilon_\infty - \frac{\omega_p^2}{\omega^2 + i\Gamma\omega} \right) \quad (7)$$

In Eq. 7  $\epsilon_0$  is the permittivity of free space and  $\epsilon_\infty = \epsilon(\omega \rightarrow \infty)$  is the dimensionless infinite frequency limit of the dielectric constant. The Drude model is based on a damped harmonic oscillator model of an electron plasma in which the electrons oscillate about positive ion centers with characteristic frequency  $\omega_p$ , subject to a phenomenological damping rate  $\Gamma$ , normally assumed to be due to electron-phonon coupling. Values for  $\Gamma$  are typically  $\sim 10^{14} \text{ s}^{-1}$ , and in fact for Au the value is  $1.02 \times 10^{14} \text{ s}^{-1}$ . For a wave propagating on the surface with group velocity  $\simeq 3 \times 10^8 \text{ ms}^{-1}$  the expected decay length  $\simeq 3 \mu\text{m}$ , consistent with the measurements and FDTD simulations.

In summary the picture that emerges from far-field interferometry and FDTD simulation studies of these simple slit-groove structures on silver and gold films is that in the near-zone of slit-groove distances, on the order of a few wavelengths, the surface wave consists of a composite of several evanescent modes all of which dissipate within this near-zone. Only the bound, stable SPP mode survives into the far-zone, and in the studies reported here we have observed essentially constant SPP amplitude out to  $12 \mu\text{m}$ , a distance limited only by our fabricated structures. Earlier measurements [2] indicate that absorption and surface roughness scattering should permit propagation lengths as far as  $\sim 80 - 100 \mu\text{m}$ .

## Acknowledgments

Support from the Ministère délégué à l’Enseignement supérieur et à la Recherche under the programme ACI-“Nanosciences-Nanotechnologies,” the Région Midi-Pyrénées [SFC/CR 02/22], and FASTNet [HPRN-CT-2002-00304] EU Research Training Network, is gratefully acknowledged. F.K. gratefully acknowledges support from the Deutsche Telekom Stiftung. Facilities of the Caltech Kavli Nanoscience Institute are also gratefully acknowledged.

- 
- [1] G. Gay, O. Alloschery, B. Viaris de Lesegno, J. Weiner, and H. Lezec, "Surface Wave Generation and Propagation on Metallic Subwavelength Structures Measured by Far-Field Interferometry," *Phys. Rev. Lett.* **96**, 213901-1-4 (2006).
  - [2] G. Gay, O. Alloschery, B. Viaris de Lesegno, C. O'Dwyer, J. Weiner and H. J. Lezec, "The optical response of nanostructured surfaces and the composite diffracted evanescent wave model," *Nature Phys.* **2**, 262-267 (2006).
  - [3] H. Raether, *Surface Plasmons on Smooth and Rough Surfaces and on Gratings*, (Springer-Verlag, Berlin, 1988).
  - [4] P. Lalanne and J. P. Hugonin, "Interaction between optical nano-objects at metallo-dielectric interfaces," *Nature Phys.* **2**, 551-556 (2006).
  - [5] G. Gay, O. Alloschery, J. Weiner, H. J. Lezec, C. O'Dwyer, M. Sukharev, and T. Seideman, "Analysis of surface waves generated on subwavelength-structured silver films," <http://arXiv.org:physics/0608116> v2 (2006).
  - [6] G. Gay, O. Alloschery, J. Weiner, H. J. Lezec, C. O'Dwyer, M. Sukharev, and T. Seideman, "The Response of Nanostructured Surfaces in the Near Field," *Nature Phys.* **2**, xxx (2006).
  - [7] Y. Xie, A. Zakharian, J. Moloney, and M. Mansuripur, "Transmission of light through slit apertures in metallic films," *Opt. Express* **12**, 6106-6121 (2004).
  - [8] Y. Xie, A. Zakharian, J. Moloney, and M. Mansuripur, "Transmission of light through a periodic array of slits in a thick metallic film," *Opt. Express* **13**, 4485-4491 (2005).
  - [9] A. Zakharian, J. Moloney, and M. Mansuripur, "Transmission of light through small elliptical apertures," *Opt. Express* **12**, 2631-2648 (2004).
  - [10] P. Johnson and R. Christy, "Optical Constants of the Noble Metals," *Phys. Rev. B* **6**, 4370-4379 (1972).
  - [11] Present experimental results. Value of  $n_{\text{surf}}$  determined from data in the far-zone
  - [12] Present FDTD simulations. Value of  $n_{\text{surf}}$  determined from FDTD simulations in the far-zone
  - [13] Measurements from Ref. [1] predominantly in the transient near-zone.
  - [14] Measurements from Ref. [2] predominantly in the transient near-zone.
  - [15] Value of  $n_{\text{surf}}$  determined from FDTD simulations of Refs. [5, 6] in the far-zone.
  - [16] H. J. Lezec and T. Thio, "Diffracted evanescent wave model for enhanced and suppressed optical transmission through subwavelength hole arrays," *Opt. Express* **12**, 3629-3651 (2004).
  - [17] Y. Xie, A. R. Zakharian, J. V. Moloney, and M. Mansuripur, "Transmission of light through periodic arrays of sub-wavelength slits in metallic hosts," *Opt. Express* **14**, 6400-6413 (2004).